ICE SHEETS

Ice sheet–free West Antarctica during peak early Oligocene glaciation

J. P. Klages[1]*, C.-D. Hillenbrand[2], S. M. Bohaty[3], U. Salzmann[4], T. Bickert[5], G. Lohmann[1,5,6], H. S. Knahl[1], P. Gierz[1], L. Niu[1], J. Titschack[5,7], G. Kuhn[1,8], T. Frederichs[5,8], J. Müller[1,5,8], T. Bauersachs[9], R. D. Larter[2], K. Hochmuth[10], W. Ehrmann[11], G. Nehrke[1], F. J. Rodríguez-Tovar[12], G. Schmiedl[13], S. Spezzaferri[14], A. Läufer[15], F. Lisker[8], T. van de Flierdt[16], A. Eisenhauer[17], G. Uenzelmann-Neben[1], O. Esper[1], J. A. Smith[2], H. Pälike[5,8], C. Spiegel[8], R. Dziadek[1], T. A. Ronge[18], T. Freudenthal[5], K. Gohl[1]

One of Earth's most fundamental climate shifts, the greenhouse-icehouse transition 34 million years ago, initiated Antarctic ice sheet buildup, influencing global climate until today. However, the extent of the ice sheet during the Early Oligocene Glacial Maximum (~33.7 to 33.2 million years ago) that immediately followed this transition—a critical knowledge gap for assessing feedbacks between permanently glaciated areas and early Cenozoic global climate reorganization—is uncertain. In this work, we present shallow-marine drilling data constraining earliest Oligocene environmental conditions on West Antarctica's Pacific margin—a key region for understanding Antarctic ice sheet evolution. These data indicate a cool-temperate environment with mild ocean and air temperatures that prevented West Antarctic Ice Sheet formation. Climate–ice sheet modeling corroborates a highly asymmetric Antarctic ice sheet, thereby revealing its differential regional response to past and future climatic change.

Plausible projections of future transitions into very different climate states require a profound understanding of the dynamics of drastic climate changes in Earth's past. One such fundamental change—i.e., from early Cenozoic greenhouse to late Cenozoic icehouse conditions—occurred across the Eocene-Oligocene transition (EOT) and is evident from a sharp, two-step increase of deep-ocean oxygen isotope ($\delta^{18}O$) values reflecting a combination of both decreasing but regionally highly variable ocean temperatures and major ice sheet buildup (*1*–*4*). The first $\delta^{18}O$ step occurred during the EOT [~34.4 to 33.7 million years ago (Ma)] (*1*–*3*), thought to be initiated by low summer insolation (*3*), whereas the second, more-prominent step—known as the early Oligocene oxygen isotope step (EOIS) (*4*) and commonly referred to as Oi-1 (*1*, *3*)—marks the end of the EOT and the start of the Early Oligocene Glacial Maximum (EOGM) (~33.7 to 33.2 Ma) (*1*, *5*). Constraints on the size, location, and timing of growth of early Antarctic ice sheets, however, remain sparse (*6*–*8*), which prevents us from assessing their impact on past global climate dynamics, including ice-ocean-atmosphere interactions during phases of substantial change (*2*).

In the Northern Hemisphere, previous studies have inferred patches of marine-terminating land-based ice on Greenland already present during the mid- to late Eocene from the deposition of ice-rafted debris (IRD) in the Norwegian-Greenland Sea (*9*) but without firm constraints on ice-mass size and location. By contrast, East Antarctic land-based ice likely grew stepwise throughout the EOT—starting from late Eocene ephemeral alpine glaciation to glacial advance toward outer shelf regions in Prydz Bay (*10*), with further evidence for contemporary iceberg rafting in both the adjacent deep sea (*11*) and the Weddell Sea region (*11*, *12*). In the Ross Sea sector, presence of grounded ice directly at the coast has not been documented before ~33 Ma (*13*). For West Antarctica, it is debated whether there was major ice sheet buildup during the EOT-EOGM (*6*, *14*, *15*) or later during the late Oligocene–early Mocene interval (*16*). Numerical models suggest that the prominent EOIS at ~33.7 Ma (*4*) is best explained by Antarctic glaciation alone, likely with a partial (*17*) or full (*7*) West Antarctic contribution. So far, however, reliable records proximal to West Antarctica that could document the presence or absence of a West Antarctic Ice Sheet (WAIS) during the EOGM are missing.

We report on drill core records from the West Antarctic margin that reveal paleoenvironmental conditions during the EOGM. Site PS104_21 (73.31°S, 107.11°W; 882-m water depth; Fig. 1) was drilled during research vessel (RV) *Polarstern* expedition PS104 in Pine Island Trough on the Amundsen Sea Embayment (ASE) shelf (*18*), with two holes (21-2 and 21-3) ~86 m apart. Seaward-dipping strata beneath the midshelf part of the trough are truncated near the seafloor by an amalgamated unconformity caused by repeated Miocene-Pleistocene cross-shelf ice advances (*19*–*21*) (Fig. 1B). These sedimentary strata were shown to be of mid-Cretaceous age at the inner-midshelf transition (*20*) and become successively younger in a seaward direction (*18*). However, the semilithified character of the dipping sequences previously prevented their recovery with conventional coring methods. This hurdle was overcome by deploying the MARUM-MeBo70 seafloor drill rig (*22*), which allowed drilling ~10 m into the seabed and sampling of the dipping, semilithified strata (*18*) (Fig. 1 and Fig. 2).

Lithology and stratigraphy

Beneath a thin layer of late Quaternary sediments, laminated semilithified muds and mudstones—interrupted by three intervals of no recovery (Fig. 2)—extend to the bottom of the ~10-m-deep hole 21-3. These strata contain both terrestrial and marine microfossils but lack any gravel-sized grains and bear only traces of terrigenous sand (Fig. 2). An ~4-m-thick sequence of identical semilithified muds and mudstones was retrieved in hole 21-2, which we correlated to hole 21-3 using lithological features and magnetic susceptibility data (fig. S1). The presence of distinct, mostly horizontally oriented trace fossils without cross-cutting relationships and absence of mottling throughout hole 21-3 indicate abundant epibenthic and shallow-endobenthic life while excluding strong vertical bioturbation of the sedimentary record by infauna (movie S1). Thin sections were prepared from two carbonate-cemented mudstone beds at ~8.78 to 8.74 meters below seafloor (mbsf) and ~3.33 to 3.23 mbsf (Fig. 2), which contain rare calcareous microfossils, such as benthic foraminifera, and indistinct microscopic fragments of terrestrial organic matter (TOM). Five samples taken within the laminated mudstone interval provided sufficient biogenic carbonate for radiogenic strontium (Sr) isotope stratigraphic dating (Fig. 2 and table S1), consistently returning latest Eocene to earliest Oligocene ages between 34.59 ± 0.2 Ma and 33.09 ± 0.2 Ma, with a mean age of 33.82 ± 0.18 Ma (fig. S2). Likely due to minor diagenetic alteration and/or syndepositional reworking from shallower seabed, these $^{87}Sr/^{86}Sr$ dates show no clear stratigraphic order, but most of them overlap within error. Based on the tight cluster of the $^{87}Sr/^{86}Sr$ ages from both above and below a magnetic reversal recorded at the top of core 3R (Fig. 2), this transition from reversed to normal polarity is correlated to the boundary between magnetic polarity

[1]Alfred-Wegener-Institut Helmholtz-Zentrum für Polar- und Meeresforschung, Bremerhaven, Germany. [2]British Antarctic Survey, Cambridge, UK. [3]Institute of Earth Sciences, University of Heidelberg, Heidelberg, Germany. [4]Department of Geography and Environmental Sciences, Northumbria University, Newcastle upon Tyne, UK. [5]MARUM – Center for Marine Environmental Sciences, Bremen, Germany. [6]Environmental Physics, University of Bremen, Bremen, Germany. [7]Marine Research Department, Senckenberg am Meer (SAM), Wilhelmshaven, Germany. [8]Faculty of Geosciences, University of Bremen, Bremen, Germany. [9]Chair of Organic Biogeochemistry in Geo-Systems, RWTH Aachen University, Aachen, Germany. [10]Australian Centre for Excellence in Antarctic Science, Institute for Marine and Antarctic Studies, University of Tasmania, Hobart, TAS, Australia. [11]Institute for Geophysics and Geology, University of Leipzig, Leipzig, Germany. [12]Departamento de Estratigrafía y Paleontología, Universidad de Granada, Granada, Spain. [13]Center for Earth System Research and Sustainability, Institute for Geology, University of Hamburg, Hamburg, Germany. [14]Department of Geosciences, University of Fribourg, Fribourg, Switzerland. [15]Polar Geology, Bundesanstalt für Geowissenschaften und Rohstoffe, Hannover, Germany. [16]Department of Earth Science and Engineering, Imperial College London, London, UK. [17]GEOMAR Helmholtz-Zentrum für Ozeanforschung Kiel, Kiel, Germany. [18]International Ocean Discovery Program, Texas A&M University, College Station, TX, USA.
*Corresponding author. Email: johann.klages@awi.de

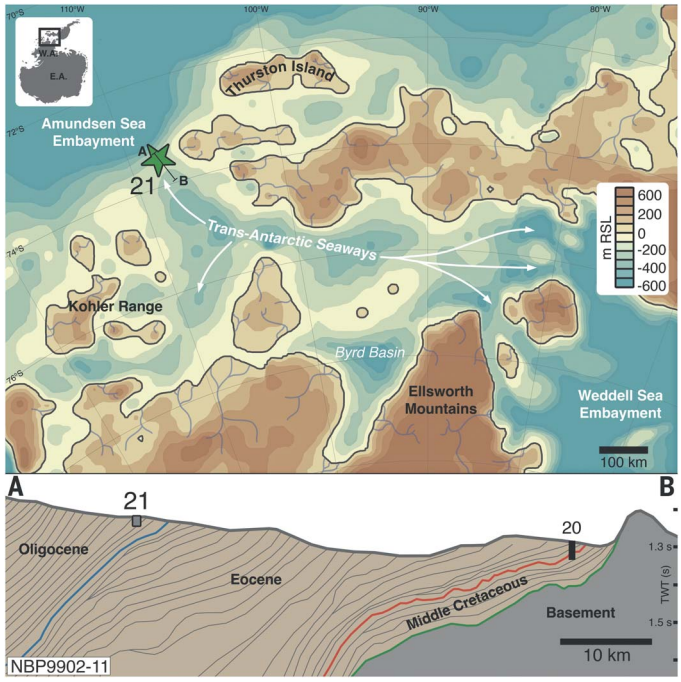

Fig. 1. West Antarctic topographic setting 34 Ma and stratigraphic context of the drill site. (**Top**) Map of the West Antarctic archipelago between the ASE and Weddell Sea at the time of the EOGM with MeBo drill site PS104_21 (green star) based on the reconstructed 34 Ma minimum bed topography from Paxman *et al.* (*38*). Locations of MeBo drill site PS104_21 (green star) and the seismic profile NBP9902-11 (line A–B) presented in the bottom panel are also shown. Positions of rivers are hypothetical and based on our interpretation of the paleoenvironmental conditions for the deposition of the PS104_21 sediments, inferred from micropaleontological and biomarker analyses (see text). RSL, relative sea level. The inset in upper left corner indicates locations of West Antarctica (W.A.), East Antarctica (E.A.), and the study area (black square). (**Bottom**) Interpretation of seismic profile NBP9902-11 (*19*, *21*) with projected position (gray) of MeBo site PS104_21 and position of MeBo site PS104_20 (*20*), which is included for further context. TWT, two-way travel time.

chrons C13r and C13n at 33.73 Ma (*23*), which corresponds to the EOIS (*4*, *24*) (fig. S2). This correlation to the geomagnetic polarity timescale is also supported by present *Bolboforma* species *Bolboforma indistincta* and *Bolboforma irregularis*, which have last and first occurrences within calcareous nannofossil zone NP21 that spans the EOT and EOGM (*25*).

Paleoenvironment and climate

Sediment cores 5R to 1R from hole PS104_21-3 (Fig. 2) and cores 3R and 2R from hole 21-2 (*26*, *27*) (fig. S1) record a marine environment evident from rare but continuous occurrences of both marine microfossils (i.e., foraminifera, dinoflagellate cysts, calcareous nannofossils, and *Bolboforma*; table S2 and fig. S3) and trace fossils (e.g., *Zoophycos*; movie S1). Dominance of benthic foraminifera, with only one planktic specimen found (table S2), designate a relatively shallow (50 to 200 m) mid- to outer-shelf environment (*28*), consistent with the presence of *Bolboforma*—an extinct group of calcareous microfossils—previously also described from water depths as shallow as 30 to 50 m (*29*). Similar benthic foraminiferal and *Bolboforma* assemblages have so far only been reported from the early Oligocene of the Victoria Land Basin (*28*) and the late Eocene-Oligocene from the eastern Australian margin (*25*), respectively. The dominance of epifaunal to shallow-infaunal benthic foraminifera species and trace fossils (table S2 and movie S1) indicates well-ventilated bottom waters but reduced oxygen penetration into the seabed, likely due to the extremely fine grain size of the sediments (Fig. 2). The benthic foraminiferal assemblage additionally points to pulses of phytodetritus and frequent influx of fresh water (*28*). This is also supported by elevated ratios of terrestrial versus aquatic-sourced short-chain hydrocarbons (TAR_{HC}) (*30*) (Fig. 2), which suggests increased influx of TOM from vegetated land, as does the presence of the trace fossil *Phycosiphon incertum* (*31*). Comparatively high branched and isoprenoid tetraether (BIT) index values of >0.5 (Fig. 2) indicate that TOM influx has mainly been facilitated by rivers and creeks (*32*) (Fig. 1). A close proximity to land is further indicated by the regular occurrence of pollen and spores of higher land plants (Fig. 2 and table S3). Low alkane $n\text{-}C_{31}/(n\text{-}C_{27} + n\text{-}C_{29} + n\text{-}C_{31})$ ratios point to prevalent deciduous trees (*30*) (fig. S4).

The fossil pollen assemblage in our record (fig. S11 and table S3) closely resembles modern pollen rain spectra from the South American subantarctic deciduous forest biome (*33*), characterized by very high percentages (>80 to 90%; table S4) of *Nothofagidites* pollen [nearest living relative (NLR): *Nothofagus*; see table S5] and regular occurrences of conifer pollen (NLR: *Podocarpus*, *Microcachryidites antarcticus*, *Araucariaceae*) and *Stereosporites* (NLR: *Sphagnum* mosses). Today, such southern beech-rich forests are abundant in Patagonia, where they thrive in a cool-temperate climate with mean annual air temperatures of ~6.0° to 8.5°C, mean summer temperatures of ~9.8° to 13.8°C, and a mean annual precipitation of >1500 mm (*33*). These vegetation-derived terrestrial temperatures are in close accordance with our TEX^{L}_{86} (tetraether index of tetraethers consisting of 86 carbon atoms) subsurface ocean temperatures (SOTs) of the archipelago, which range from ~6.2° to ~10.5°C (±2.8°C calibration error; Fig. 2 and Fig. 3). Comparatively high BIT and ring index (ΔRI) values may additionally bias TEX^{L}_{86}-based temperature reconstructions—i.e., ±2.9°C in sediments receiving higher amounts of TOM (see materials and methods in the supplementary materials for applying the TEX^{L}_{86} calibration despite high BIT values). The occasional dissolution of resistant *Bolboforma* specimens (fig. S3, D to F) indicates that seawater temperatures may have periodically dropped to 5°C or less throughout the year (*34*). In general, those temperatures would have been too high to allow any presence of permanent marine-terminating ice. Moreover, the predominance of subangular to rounded quartz grains in the sand fraction throughout the PS104_21 record, including grains with shiny surfaces and medium-to-high sphericities (Fig. 2), argues against their glacial erosion and subglacial transport. Instead, these grain characteristics are more indicative of fluvial transport (*35*) on nearby land, thus corroborating our interpretation of the foraminiferal assemblage and BIT index. Furthermore, the lack of clastic grains >2 mm, commonly used as IRD proxy (*36*), in the fine-grained sediments at this location (Fig. 2) indicates that land-based ice was absent from the coastal region near the site. Additionally, very low contents of kaolinite (~5%; Fig. 2) may further support a WAIS-free scenario because subglacial erosion in the Byrd Subglacial Basin is considered to be the main source for kaolinite in modern and late Quaternary ASE sediments (*37*).

The PS104_21 record clearly documents a marine depositional setting, hence validating the minimum Antarctic bed topography reconstruction for 34 Ma proposed by Paxman *et al.* (*38*) for this part of West Antarctica as opposed to their medium and maximum scenarios, in which the entire area around site PS104_21 is land (*38*). Our findings suggest that parts of West Antarctica must have already been

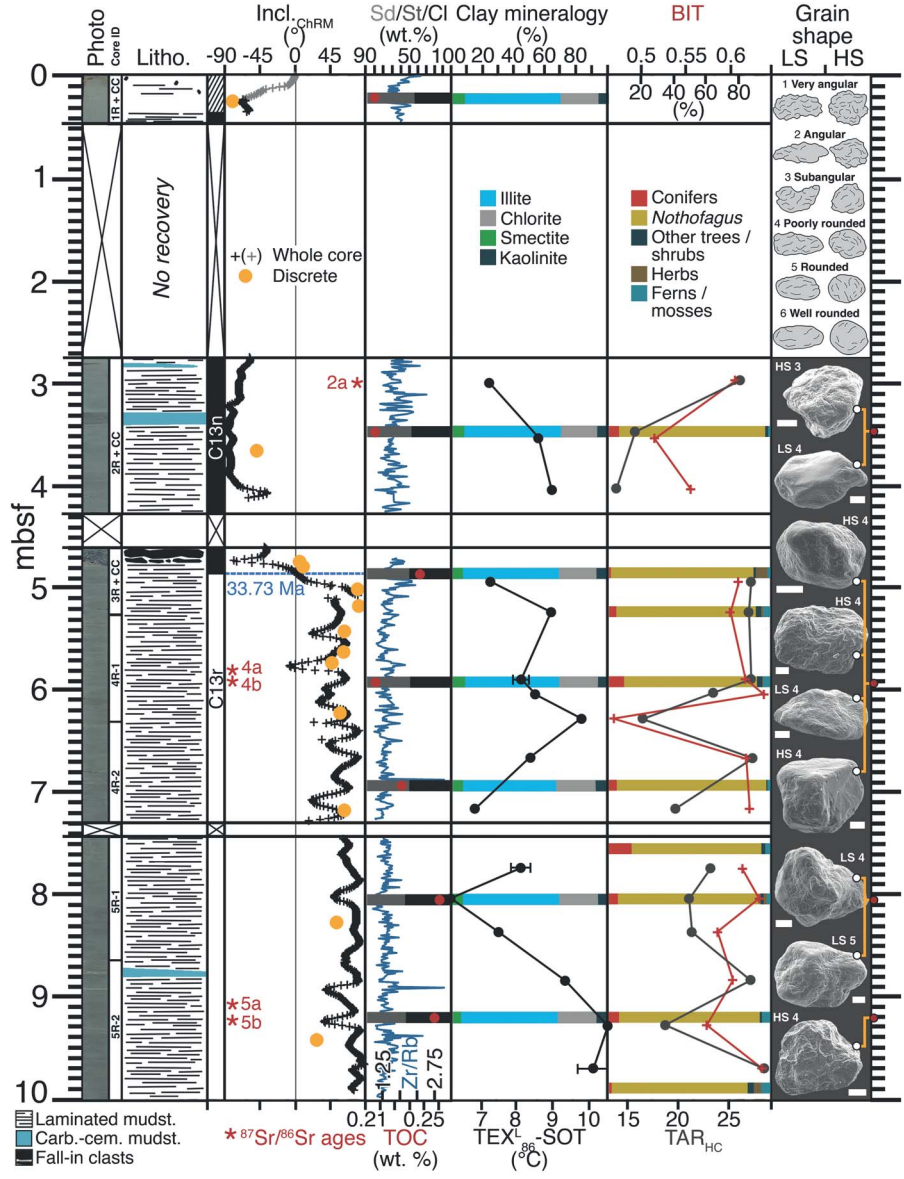

Fig. 2. Multiproxy results from MeBo drill site 21-3. Core photos, lithology, magnetic inclination data (measured on whole cores and discrete samples), various environmental proxies, and scanning electron microscope (SEM) images of sand-sized quartz grains (sample depths indicated by yellow brackets) from cores 1R to 5R of hole PS104_21-3 (*27*). The MARUM-MeBo70 seafloor drill rig penetrated 10 m into the seabed and recovered 7.34 m of core (73.4%). An ~4-cm-thin drape of Holocene unconsolidated sandy mud was recovered just beneath the seafloor, and an ~1.1-m-long sequence of bioturbated to laminated mud and sandy mud overlying structureless diamicton—probably reflecting deposition since the Last Glacial Maximum (LGM)—was retrieved in hole PS104_21-2 and gravity core PS104_21-1 from the same location. The sediments below the Holocene sandy mud in hole PS104_21-3 consist of ~7.30 m of laminated semilithified mud and mudstone of earliest Oligocene age. Two carbonate-cemented mudstone beds occur at ~8.78 to 8.74 mbsf and ~3.33 to 3.23 mbsf. Sampling depths and associated sample numbers for strontium isotope ($^{87}Sr/^{86}Sr$) dating are indicated by red stars with results given in table S1 and fig. S2. C13r and C13n, magnetic polarity chrons; $Incl._{ChRM}$, inclination values of characteristic remanent magnetization (see materials and methods); Sd/St/Cl, sand/silt/clay; Zr/Rb: zirconium/rubidium ratio (grain-size proxy); TOC, total organic carbon; TEX^{L}_{86}-SOT, TEX^{L}_{86} subsurface ocean temperatures (error bars indicate analytical error for replicated samples); LS, low sphericity; HS, high sphericity.

situated below sea level during the EOGM, potentially allowing the existence of open trans-Antarctic seaways (Fig. 1). This interpretation is supported by recent findings of reworked Paleogene open-ocean microfossils in modern subglacial sediments from the Siple and Gould coasts in the Ross Sea sector (*39*). Overall, we infer that during peak early Oligocene glaciation, the coasts of West Antarctica's Amundsen Sea sector were still covered by cool-temperate forests without evidence for marine-terminating ice. Hence, any large permanent West Antarctic ice mass must have been very distant or did not exist until after the EOGM, which implies that deep-sea cooling may have had a larger impact on the EOGM $\delta^{18}O$ signature in benthic foraminifera than previously thought.

Paleoenvironmental modeling

Our data constraints contradict results of previous model simulations that included a fully developed, marine-terminating WAIS during the EOGM [~2x preindustrial (PI) CO_2] (*3*, *7*) (Fig. 3) and support model outputs implying limited West Antarctic ice coverage (*40*). However, available models differ considerably in simulating the amount of ice (*7*, *17*, *40*, *41*), mainly because of the scarcity of field data and associated uncertainties in bed topography reconstructions (*38*). In this work, we use the state-of-the-art Alfred Wegener Institute–Earth System Model (AWI-ESM-2.1-LR) asynchronously coupled to the Parallel Ice Sheet Model (PISM) (materials and methods) to further explore the consequences of a vegetated and ice sheet–free West Antarctica that we reconstructed for the EOGM. AWI-ESM-2.1-LR consists of fully coupled atmosphere, ocean, and sea ice components (*42*), supplemented by the land-surface and vegetation module JSBACH. The asynchronously coupled experiment was run into quasi-equilibrium state (1500 climate years and 200,000 ice years; fig. S5, E to G). For our simulation, we used the reconstructed minimum bed topography (*38*) as a boundary condition (fig. S5A) because only this reconstruction is consistent with our multiproxy record from West Antarctica's Pacific margin.

Our multiproxy evidence closes a critical West Antarctic gap in paleoenvironmental data for the earliest Oligocene (Fig. 3). To upscale the regional signal, we further combined our results with environmental data from other circum-Antarctic records spanning the earliest Oligocene interval (~33.9 to 31.0 Ma) (Fig. 3 and table S6). With that, we obtain an earliest Oligocene continent-wide context for comparing our EOGM ice sheet and climate reconstruction from site PS104_21 with climate model results. We specifically ran our simulation with the reconstructed atmospheric CO_2 concentration of ~850 parts per million by volume (ppmv), representing latest Eocene conditions just before the EOGM (*43*) (~3x PI CO_2; Fig. 4). Reconstructed surface air and ocean temperatures for the EOGM reveal a clear pattern, with warmer conditions in the southwestern Pacific and along the Wilkes Land margin (Fig. 3). Considering the uncertainties for both temperature reconstructions (including analytical and calibration errors) and Earth system modeling (e.g., gateway bathymetry, orbital configuration, and deep-water formation) at high

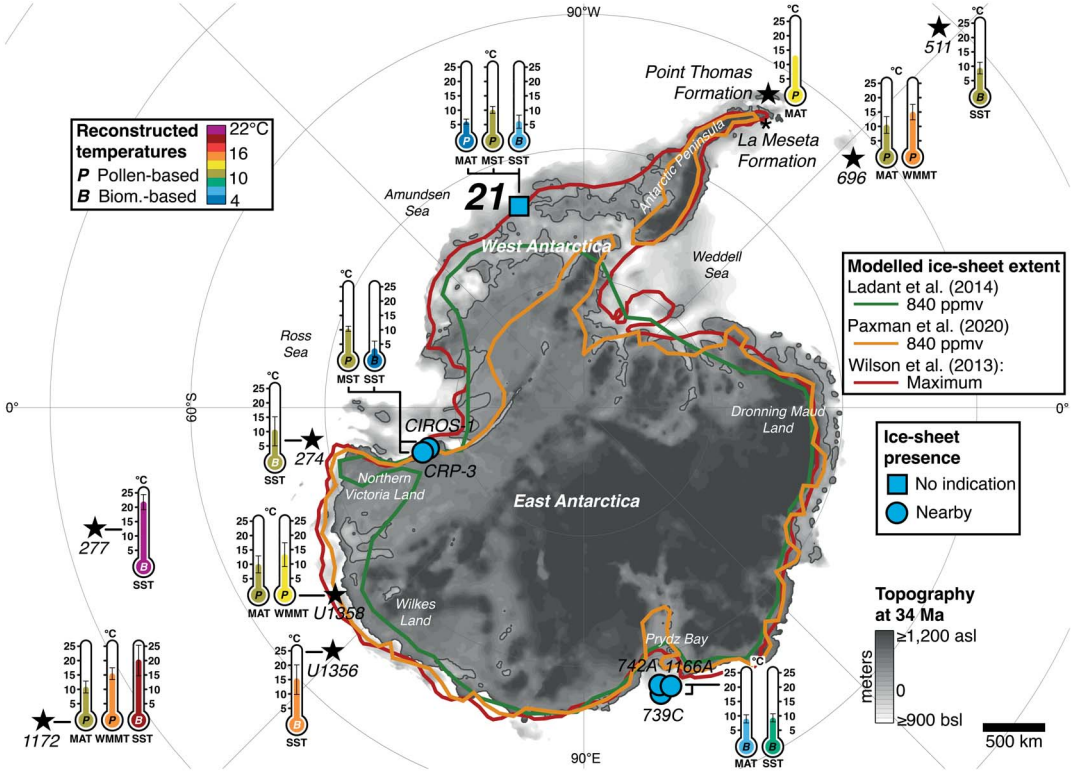

Fig. 3. Circum-Antarctic paleoenvironmental data evidence and previous modeling scenarios for earliest Oligocene Antarctic ice sheet extent. Existing earliest Oligocene (33.9 to 31 Ma) data records around Antarctica for terrestrial and sea-surface temperatures and ice presence (Point Thomas and La Meseta formations are exposed on land). Available pollen- (*P*) or biomarker-based (*B*) temperature proxy results are shown separately for each site (MAT, mean annual temperature; MST, mean summer temperature; WMMT, warmest mean month temperature; SST, sea-surface temperature) and indicate coldest values, including analytical uncertainties in the 33.9 to 31 Ma period. Sites with available data for ice presence or absence are marked by the blue icons referenced within the figure; all other sites are indicated by black stars. Only the La Meseta Formation is indicated by an asterisk because ice sheet presence is under debate (*14*, *15*). The green, red, and orange outlines refer to different modeled ice sheet extents at the EOGM (*3*, *7*, *40*). All data visualized here are listed in more detail and referenced in table S6. The minimum topography reconstruction from Paxman *et al.* (*38*) was used. asl, above sea level; bsl, below sea level.

latitudes, our compiled proxy temperature data for the earliest Oligocene (Fig. 3 and table S6) best match simulated temperatures that were initiated with 3x PI CO_2 conditions (~850 ppmv; Fig. 4, B and C, and fig. S5). This is consistent with recently revised CO_2 reconstructions from marine proxies across the EOT, which average 800 to 1000 ppmv in the late Eocene and decrease to ~600 ppmv after the EOT (*43*), although neither the exact timing nor the absolute CO_2 concentration of the earliest Oligocene minimum are well constrained. Under such climate conditions, our simulation is also consistent with earliest Oligocene data constraints on ice sheet extent in Prydz Bay (*10*) and the western Ross Sea (*13*, *44*) (Fig. 4A). However, our model simulates an ice sheet–free West Antarctica not only for 3x PI CO_2 but also for 2x PI CO_2 conditions (Fig. 4, A and E). Both simulated scenarios therefore agree with our data interpretation from site PS104_21 that West Antarctica remained ice sheet–free during the EOGM and exhibit a West Antarctic biome (Fig. 4D and fig. S7) that matches well with our reconstructed vegetation (Fig. 2) and climate. Moreover, the results predict a potential ice sheet nucleus close to the coast of northern Victoria Land (fig. S6D and materials and methods), near a location in the Ross Sea where geological evidence documents the presence of grounded ice as early as 33.0 Ma and its proximity since at least 33.3 Ma (*13*, *44*, *45*). This nucleus—in contrast to, for example, the Gamburtsev Mountains in the continent's dry interior—was likely initiated by increased precipitation (fig. S7) from moist air masses originating from warm waters that reached the rapidly uplifting and already >1500- to 2000-m-high Transantarctic Mountains (*46*) (Fig. 3 and white arrows in fig. S5) and possibly flowed through an open, but yet shallow, Tasman Gateway (*47*). This led to increased precipitation and prominent ice cap formation over northern Victoria Land.

Overall, our model results imply that growth and expansion of a marine-terminating ice sheet in West Antarctica occurred much later than in East Antarctica (*10*, *13*). Ice advances reaching the West Antarctic coast initiated only at lower atmospheric CO_2 levels between ~560 ppmv and 280 ppmv (fig. S6, A and B)—values first recorded after ~26 Ma in the late Oligocene (*43*), when Antarctica's thermal isolation had progressed further (*47*). For the EOGM, we calculate a total Antarctic ice volume between 1.66 and 1.45 × 10^7 km^3 (38.0 to 32.5 m sea level equivalent) (Fig. 4A and fig. S6B), which aligns with minimum volume estimates calculated from deep-sea foraminiferal $\delta^{18}O$ and Mg/Ca data for the EOGM interval (*5*). Marine-terminating ice advance in the Amundsen Sea sector was likely delayed by subdued topography as well as prevailing mild air and surface ocean temperatures in this region (as shown by our PS104_21 record) but was initiated earlier in the Ross Sea sector (fig. S6, A and B). In the ASE, warmer waters may have reached the low-lying archipelago from lower latitudes as a consequence of yet shallow configurations of both the Tasman Gateway and Drake Passage (*47*), which affected this area for much longer than assumed until recently (*48*). Hence, our climate–ice sheet simulation is entirely consistent with our well-dated multiproxy record, which indicated an ice sheet–free West Antarctica throughout the EOGM. Strongly reduced ice-associated climate feedbacks, such as albedo, likely further helped to maintain regional warmth and associated circulation patterns in the atmosphere and ocean (*49*).

We conclude that a large but not continent-wide ice sheet existed only in East Antarctica during the initial phase of the Cenozoic icehouse. Our results match previous EOGM ice sheet volume estimates (*4*, *5*, *24*) and suggest initial WAIS expansion into marine basins when atmospheric CO_2 concentrations began to fall below ~560 ppmv—i.e., at least ~7 million years later in the late Oligocene (*43*). Hence, our combined multiproxy data and climate–ice sheet simulation reveal a highly asymmetric behavior of the Antarctic ice sheet, providing essential insight for understanding its response during past and future climate reorganizations.

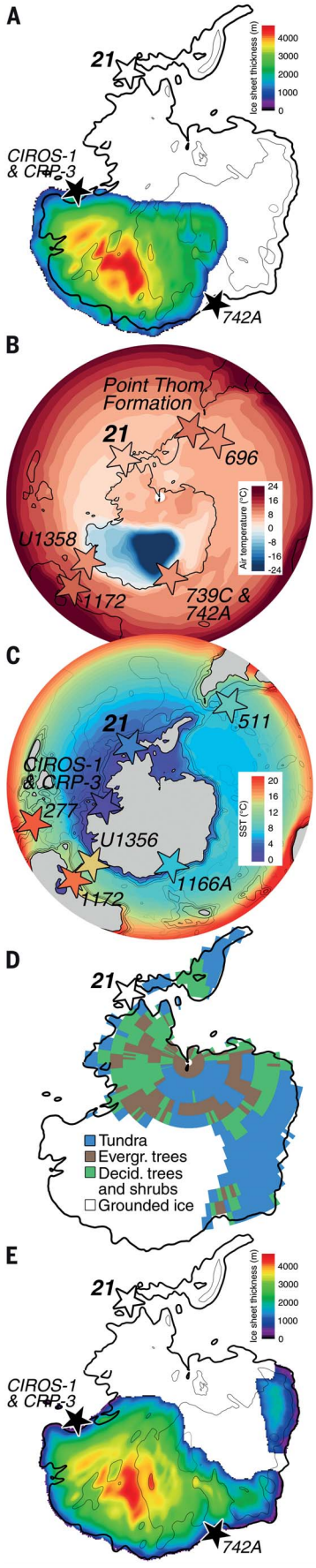

Fig. 4. Results of ice sheet and Earth system modeling compared with paleo-data records. (**A** to **D**) Simulated Antarctic environment for 840 ppmv (3x PI) atmospheric CO_2 forcing compared with available data. Ice sheet configuration 200,000 years after ice-free conditions (A) with the corresponding EOGM climate showing air temperatures at 2 m height (B), sea-surface temperature (C), and vegetation cover (D). Evergr., evergreen; Decid., deciduous. (**E**) Ice sheet configuration under 2x PI CO_2 conditions (fig. S6). Sites indicating ice presence in (A) are highlighted by filled black stars, whereas a white star with a black outline marks site PS104_21 without indication for glacial ice. Stars in (B) and (C) indicate the locations of drill sites providing surface air MATs and SSTs, respectively, with their fill color indicating the reconstructed temperature (Fig. 3 and table S6). Colors in (A) refer to ice thickness above bedrock, and black isolines indicate the minimum 34 Ma bed topography reconstruction (*38*).

REFERENCES AND NOTES

1. J. Zachos, M. Pagani, L. Sloan, E. Thomas, K. Billups, *Science* **292**, 686–693 (2001).
2. T. Westerhold *et al*., *Science* **369**, 1383–1387 (2020).
3. J.-B. Ladant, Y. Donnadieu, V. Lefebvre, C. Dumas, *Paleoceanography* **29**, 810–823 (2014).
4. D. K. Hutchinson *et al*., *Clim. Past* **17**, 269–315 (2021).
5. S. M. Bohaty, J. C. Zachos, M. L. Delaney, *Earth Planet. Sci. Lett.* **317-318**, 251–261 (2012).
6. S. Galeotti *et al*., in *Antarctic Climate Evolution*, F. Florindo, M. Siegert, L. De Santis, T. Naish, Eds. (Elsevier, ed. 2, 2022), pp. 297–361.
7. D. S. Wilson, D. Pollard, R. M. DeConto, S. S. R. Jamieson, B. P. Luyendyk, *Geophys. Res. Lett.* **40**, 4305–4309 (2013).
8. Z. Liu *et al*., *Science* **323**, 1187–1190 (2009).
9. J. S. Eldrett, I. C. Harding, P. A. Wilson, E. Butler, A. P. Roberts, *Nature* **446**, 176–179 (2007).
10. S. Passchier, D. J. Ciarletta, T. E. Miriagos, P. K. Bijl, S. M. Bohaty, *Geol. Soc. Am. Bull.* **129**, 318–330 (2017).
11. W. Ehrmann, A. Mackensen, *Palaeogeogr. Palaeoclimatol. Palaeoecol.* **93**, 85–112 (1992).
12. A. Carter, T. R. Riley, C.-D. Hillenbrand, M. Rittner, *Earth Planet. Sci. Lett.* **458**, 49–57 (2017).
13. S. Galeotti *et al*., *Science* **352**, 76–80 (2016).
14. S. A. Marenssi, S. Casadío, S. N. Santillana, *Antarct. Sci.* **22**, 193–198 (2010).
15. L. C. Ivany, S. Van Simaeys, E. W. Domack, S. D. Samson, *Geology* **34**, 377–380 (2006).
16. J. W. Marschalek *et al*., *Nature* **600**, 450–455 (2021).
17. R. M. Deconto *et al*., *Nature* **455**, 652–656 (2008).
18. K. Gohl *et al*., *Geochem. Geophys. Geosyst.* **18**, 4235–4250 (2017).
19. A. L. Lowe, J. B. Anderson, *Quat. Sci. Rev.* **21**, 1879–1897 (2002).
20. J. P. Klages *et al*., *Nature* **580**, 81–86 (2020).
21. K. Gohl *et al*., *Mar. Geol.* **344**, 115–131 (2013).
22. T. Freudenthal, G. Wefer, *Geosci. Instrum. Methods Data Syst.* **2**, 329–337 (2013).
23. F. M. Gradstein, J. G. Ogg, M. D. Schmitz, G. M. Ogg, Eds., *Geologic Time Scale 2020* (Elsevier, ed. 1, 2020).
24. L. Diester-Haass, R. Zahn, *Geology* **24**, 163–166 (1996).
25. D. Spiegler, S. Spezzaferri, *Palaontol. Z.* **79**, 167–181 (2005).
26. J. P. Klages *et al*., Palynological, palaeomagnetic, and sediment physical investigations of cores 1R to 3R from MARUM-MeBo70 Site PS104_21-2 [dataset bundled publication], *PANGAEA* (2022); https://doi.org/10.1594/PANGAEA.940329.
27. J. P. Klages *et al*., Sedimentological, palynological, geochemical, palaeomagnetic, geochronological, and sediment physical investigations of cores 1R to 5R from MARUM-MeBo70 Site PS104_21-3 [dataset bundled publication], *PANGAEA* (2022); https://doi.org/10.1594/PANGAEA.940344.
28. C. P. Strong, P.-N. Webb, *Terra Ant.* **8**, 347–358 (2001).
29. C. W. Poag, A. L. Karowe, *Palaios* **1**, 162–171 (1986).
30. P. A. Meyers, *Org. Geochem.* **34**, 261–289 (2003).
31. F. J. Rodríguez-Tovar, J. Nagy, M. Reolid, *Polar Res.* **33**, 23786 (2014).
32. E. C. Hopmans *et al*., *Earth Planet. Sci. Lett.* **224**, 107–116 (2004).
33. V. Montade, O. Peyron, C. Favier, J. P. Francois, S. G. Haberle, *J. Quaternary Sci.* **34**, 76–86 (2019).
34. J.-D. Naviaux *et al*., *Geochim. Cosmochim. Acta* **246**, 363–384 (2019).
35. K. Vos, N. Vandenberghe, J. Elsen, *Earth Sci. Rev.* **128**, 93–104 (2014).
36. H. Grobe, *Polarforschung* **57**, 123–126 (1987).
37. W. Ehrmann *et al*., *Antarct. Sci.* **23**, 471–486 (2011).
38. G. J. G. Paxman *et al*., *Palaeogeogr. Palaeoclimatol. Palaeoecol.* **535**, 109346 (2019).
39. J. J. Coenen *et al*., *Geophys. Res. Lett.* **47**, e2019GL085281 (2020).
40. G. J. G. Paxman, E. G. W. Gasson, S. S. R. Jamieson, M. J. Bentley, F. Ferraccioli, *Geophys. Res. Lett.* **47**, e2020GL09000 (2020).
41. J. Van Breedam, P. Huybrechts, M. Crucifix, *Earth Planet. Sci. Lett.* **586**, 117532 (2022).
42. M. Kageyama *et al*., *Clim. Past* **17**, 1065–1089 (2021).
43. Cenozoic CO_2 Proxy Integration Project ($CenCO_2PIP$) Consortium, *Science* **382**, eadi5177 (2023).
44. C. R. Fielding, T. R. Naish, K. J. Woolfe, *Terra Ant.* **8**, 217–224 (2001).
45. S. Galeotti *et al*., *Palaeogeogr. Palaeoclimatol. Palaeoecol.* **335–336**, 84–94 (2012).
46. J. Prenzel *et al*., *Gondwana Res.* **53**, 110–128 (2018).
47. I. Sauermilch *et al*., *Nat. Commun.* **12**, 6465 (2021).
48. G. Uenzelmann-Neben *et al*., *Commun. Earth Environ.* **3**, 36 (2022).
49. N. Wunderling, M. Willeit, J. F. Donges, R. Winkelmann, *Nat. Commun.* **11**, 5177 (2020).
50. H. S. Knahl, L. Niu, G. Lohmann, P. Gierz, J. P. Klages, Source codes of AWIESM with interactive ice sheet model PISM, Zenodo (2024); https://doi.org/10.5281/zenodo.10808075.

ACKNOWLEDGMENTS

We thank the captain and crew of RV *Polarstern* Expedition PS104 as well as the MARUM- *MeBo70* team for their support. V. Afanasyeva, J. E. Arndt, C. Gebhardt, Y. Najman, P. Simões Pereira, F. Riefstahl, M. Scheinert, K. Küssner, and M. Zundel were part of the Science Team of Expedition PS104 and are thanked for their help on board and in the laboratory. S. Wiebe, R. Fröhlking, V. Schumacher, N. Lensch, M. Arevalo, M. Kuck, D. Diekstall, M. Seebeck, and R. Cordelair are thanked for technical support on board and in the laboratory. The *Klinikum Bremen-Mitte* (A.-J. Lemke and C. Tiemann, *Gesundheit Nord* Bremen) is acknowledged for providing facilities for computed core tomographies, and M. Köhler (MKfactory, Germany) as well as C. Schott (University of Bremen, Germany) are acknowledged for preparing the thin sections. S. S. R. Jamieson (University of Durham, UK) is thanked for advice on initial ice presettings for the model. We are grateful to K. Worm and C. Rolf (LIAG Hannover, Service Area Grubenhagen) for providing access to the long-core cryogenic magnetometer. We further thank B. Diekmann for commenting on an earlier version of this manuscript and S. Schumacher for PANGAEA data curation. **Funding:** The operation of the MARUM-MeBo70 seafloor drill rig was funded by the Alfred Wegener Institute (AWI) through its Research Program PACES II Topic 3 and grant no. AWI_PS104_001, the MARUM Center for Marine Environmental Sciences, the British Antarctic Survey through its Polar Science for Planet Earth program, and the Natural Environment Research Council (NERC) funded UK IODP program. J.P.K., K.G., G.K., G.L., H.S.K., L.N., P.G., J.M., G.N., G.U.-N., and O.E. were funded by the AWI PACES II and the Helmholtz Association "Changing Earth – Sustaining our future" program. J.P.K. and J.M. were additionally funded through the Helmholtz Association (PD-201 and VH-NG-1101). C.-D.H., R.D.L., and J.A.S. were funded by NERC. UK IODP funded participation of T.v.d.F. and S.M.B. in expedition PS104. J.T. was funded through the Cluster of Excellence "The Ocean Floor – Earth's Uncharted Interface" at the University of Bremen. S.S. received funding for *Bolboforma* investigations from the Swiss National Science Foundation (grant no. 200020_201106). **Author contributions:** J.P.K. led the study and, together with C.-D.H., S.M.B., U.S., and K.G., conceived the idea for the study and wrote the manuscript. T.Freu., J.P.K., T.Bi., C.-D.H., S.M.B., J.A.S., K.G., T.v.d.F., W.E., O.E., and H.P. collected the cores. J.P.K., C.-D.H., T.Bi., and G.K. undertook the sedimentological analyses; U.S. and S.M.B. the micropaleontological and biostratigraphic analyses; and G.S. and S.S. the identification and interpretation of calcareous microfossils. T.Bi. and G.K. conducted the x-ray fluorescence scanning and processing of the cores. G.K. and J.P.K. carried out the grain-size and -shape analyses. J.T. led the computed tomography (CT) scanning, processing, and visualization. J.T., F.J.R.-T., and J.P.K. interpreted the CT data. J.M. and T.Ba. performed the biomarker analyses. T.Fred. conducted the paleomagnetic measurements. A.E. led the strontium isotope dating. G.N., G.K., J.P.K., and C.S. investigated the thin sections. W.E. analyzed the clay mineral assemblages. G.L., H.S.K., P.G., and L.N. undertook the modeling with AWI-ESM 2.1 and PISM. K.H., K.G., F.L., and A.L. helped improving the paleotopography as boundary condition for the model. J.P.K., T.Bi., C.-D.H., S.M.B., T.Fred., W.E., J.A.S., O.E., H.P., R.D., and T.A.R. helped with sampling and scanning the cores. K.G., G.U.-N., and R.D.L. undertook the seismic site survey. All members of the Expedition PS104 Science Team helped in pre–site survey investigations, core recovery, on-board analyses, and/or shore-based measurements. K.G., G.K., R.D.L., G.U.-N., T.Bi., and C.-D.H. acquired funding for, proposed, and planned RV *Polarstern* expedition PS104. All coauthors commented on the manuscript and provided input to its final version. **Competing interests:** The authors declare that they have no competing interests. **Data and materials availability:** All data are available online in the Data Publisher for Earth and Environmental Science (PANGAEA) (*26*, *27*). The source codes of the Alfred Wegener Institute–Earth System Model 2.1 (AWI-ESM 2.1) and the Parallel Ice Sheet Model (PISM) are available at Zenodo (*50*).

SUPPLEMENTARY MATERIALS

science.org/doi/10.1126/science.adj3931
Materials and Methods
Figs. S1 to S11
Tables S1 to S6
References (*51*–*106*)
Movie S1

Submitted 4 July 2023; accepted 10 June 2024
Published online 4 July 2024
10.1126/science.adj3931